

Cite this: *J. Mater. Chem. A*, 2020, **8**,
23293

Enhancing surface oxygen retention through theory-guided doping selection in $\text{Li}_{1-x}\text{NiO}_2$ for next-generation lithium-ion batteries†

Jianli Cheng,^{ab} Linqin Mu,^c Chunyang Wang,^d Zhijie Yang,^c Huolin L. Xin,^d Feng Lin^c and Kristin A. Persson^{*ab}

Layered lithium metal oxides have become the cathode of choice for state-of-the-art Li-ion batteries (LIBs), particularly those with high Ni content. However, the Ni-rich cathode materials suffer from extensive oxygen evolution, which contributes to the formation of surface rocksalt phases as well as thermal instability. Using first-principles calculations, we systematically evaluate the effectiveness of doping elements to enhance surface oxygen retention of $\text{Li}_{1-x}\text{NiO}_2$. The evaluation process includes (i) choosing the most stable surface facet from the perspective of equilibrium surface stability analysis of as-synthesized LiNiO_2 , (ii) determining the preferable atomic site and segregation behavior for each dopant, and (iii) evaluating the surface oxygen retention ability of doped- $\text{Li}_{1-x}\text{NiO}_2$ ($0.25 \leq x \leq 1$) compared to the pristine material. We also discuss and rationalize the ability of these elements to enhance surface oxygen retention based on local environment descriptors such as dopant–oxygen bond strength. Overall, W, Sb, Ta and Ti are predicted as the most promising surface dopants due to their strong oxygen bonds and robust surface segregation behavior. Finally, Sb-doped LiNiO_2 is synthesized and shown to present a surface enrichment of Sb and a significantly improved electrochemical performance, comparing with pristine LiNiO_2 . This work provides a generic approach that can lead to the greatly enhanced stabilization of all high-energy cathode materials, particularly the high Ni and low Co oxides.

Received 6th August 2020
Accepted 13th October 2020

DOI: 10.1039/d0ta07706b

rsc.li/materials-a

1 Introduction

Rechargeable lithium-ion batteries (LIBs) have become the ubiquitous power source for portable electronic devices, electric vehicles and grid electricity storage. Since its successful commercialization in 1990, LiCoO_2 is the cathode of choice for the majority of commercial LIBs because of its relatively high theoretical capacity ($\sim 270 \text{ mA h g}^{-1}$), high operating voltage ($\sim 3.6 \text{ V vs. Li}^+/\text{Li}$) and superb energy content per unit volume.¹ However, commercial LiCoO_2 only exhibits about 60% of its theoretical capacity due to its low thermal stability and capacity fade at high states-of-charge ($V > 4.35 \text{ V}$).² In addition, the potential risks associated with the supply of Co due to geographical concentration of mining and refining³ have shifted the research focus to other layered transition metal oxide

cathodes, specifically $\text{Li}[\text{Ni}_{1-x-y}\text{Co}_x\text{Al}_y]\text{O}_2$ (NCA) and $\text{Li}[\text{Ni}_{1-x-y}\text{Co}_x\text{Mn}_y]\text{O}_2$ (NCM).^{4,5}

To increase specific discharge capacity and total residual lithium content, the fraction of Co, Mn and Al in NCA and NCM has been progressively replaced by Ni.⁶ LiNiO_2 , one end member of the NCA and NCM series, exhibits the highest theoretical capacity (275 mA h g^{-1}) and same crystal structure with LiCoO_2 . However, widespread application of Ni-rich cathode materials is limited by their insufficient capacity retention and thermal stability.^{6,7} $\text{Li}_{1-x}\text{NiO}_2$ undergoes several reversible phase transitions during Li^+ intercalation and deintercalation,^{8–10} whereof one, at high state-of-charge ($V > 4.1 \text{ V}$), leads to a significant shrinkage of the material in the *c*-axis direction¹¹ and hence incurs extensive structural damage from the repeated lattice contraction and expansion.¹² The developed cracks expose fresh cathode surface area to the electrolyte, thus accelerating detrimental, parasitic reactions.^{13,14} Furthermore, higher Ni-content cathodes experience increased oxygen evolution, such that, for example, the amount of oxygen release was found to increase from 18.4% to 51.7% when Ni concentration was increased from 1/3 to 0.85.⁶ Surface oxygen loss also correlates with surface cation densification and phase transformation from the pristine rhombohedral phase into an ionically insulating rock salt phase.¹⁵ A thermal gravimetric analysis revealed that the phase transformation can occur at a lower

^aDepartment of Materials Science and Engineering, University of California, Berkeley, CA 94720-1760, USA

^bEnergy Storage and Distributed Resources Division, Lawrence Berkeley National Laboratory, Berkeley, CA 94720, USA. E-mail: kapersson@lbl.gov

^cDepartment of Chemistry, Virginia Tech, Blacksburg, Virginia 24061, USA

^dDepartment of Physics and Astronomy, University of California, Irvine, CA 92697, USA

† Electronic supplementary information (ESI) available. See DOI: 10.1039/d0ta07706b



temperature with increasing Ni content in NCMs.⁶ In addition, while we anticipate bulk cathode oxygen migration to be sluggish, it is possible for surface oxygen vacancies to migrate into the interior of the cathode particle; triggered by the outward diffusion of oxidized oxygen ion.¹⁶ Previous work has shown that the injection of surface oxygen vacancies into the bulk lattice of the cathode leads to severe structural degradation and cycling instability of Li-ion cathode materials.¹⁷ As a result, surface oxygen evolution not only jeopardizes the thermal stability and safety of the LIBs, but also deteriorates capacity retention.^{18–20} Therefore, improved stabilization of Ni-rich cathode surfaces is indispensable to achieve a highly stable and safe performance of future, high-energy-density LIBs.

A popular strategy to stabilize Ni-rich cathodes is by elemental doping. Depending on the selected dopant, the functionalities proposed to explain the improved cycling performance include:

- (1) Reduced phase transitions and improved mechanical property: Na,²¹ K,²² Rb,²³ Mg,²⁴ Y,²⁵ Al,²⁶ Zr,²⁷ Ga,²⁸ B,²⁹ Ti³⁰
- (2) Reduced cation mixing: Na,²¹ K,²² Rb,²³ Zr,²⁷ V³¹
- (3) Decreased oxygen loss or increased thermal stability: W,³² Y,²⁵ Sb,³³ Ti,³⁴ Zr,³⁵
- (4) Reduced acid-mediated parasitic reactions: Mo,³⁶ W,³² F³⁷.

Generally, the impact of dopants is challenging to deconvolute, as any addition to the active electrode material affect its operational performance in a multitude of ways at different length scales depending on how the dopant incorporates. Ionic conductivity, electronic state, redox compensation, bulk as well as surface phase transformation behavior and mechanical properties are all potentially influenced and inter-related. In this respect, first-principles modeling can provide a highly useful tool, as many such processes can be interrogated separately, as a function of dopant chemistry and site preference. For example, Liang *et al.* studied Al, Ga, Mg, Si, Ti, V and Zr doping effects on phase instability, Li–Ni exchange, Ni segregation, lattice distortion and oxygen evolution of Ni-rich $\text{LiNi}_{1-2y}\text{Co}_y\text{Mn}_y\text{O}_2$ ($y \leq 0.1$) cathode.³⁸ They suggested a comprehensive mitigation strategy for Ni-rich layered cathodes is unlikely to be satisfied by a single dopant species and hence proposed a multicomponent-doping strategy to improve the electrochemical performance of NCMs. Similarly, Min *et al.* suggested Al doping to suppress oxygen evolution and Mg doping to prevent cation disordering in $\text{LiNi}_{0.8}\text{Co}_{0.1}\text{Mn}_{0.1}\text{O}_2$.³⁹ In addition, oxygen evolution in LiNiO_2 was found to be thermodynamically favorable but kinetically hindered in the bulk phase.⁴⁰ However, under-coordinated surface regions are likely to facilitate oxygen kinetics, promote oxygen loss and result in the formation of surface densified phases.⁴¹

Recently, Shin *et al.*⁴² applied a high-throughput computational screening to guide the selection of the promising cation dopant to alleviate surface oxygen loss in Li-rich, Mn-rich cathode and identified Os, Sb, Ru, Ir and Ta as the top candidates.⁴² Ta was experimentally validated to improve electrochemical performance and oxygen retention. Following a similar procedure, in this work we systematically evaluate the effectiveness of doping elements to enhance surface oxygen retention of $\text{Li}_{1-x}\text{NiO}_2$, which shares many structural and

electrochemical properties with Ni-rich NCA and NCM materials. Based on previously proposed dopants for Ni-rich layered oxide cathode materials, we select eight doping candidates: W^{6+} , Sb^{5+} , Ta^{5+} , Ti^{4+} , Y^{3+} , Al^{3+} , B^{3+} and Mg^{2+} . The evaluation process includes (i) identifying the most stable surface facet of LiNiO_2 , (ii) determining the preferable atomic site and segregation behavior for each dopant, and (iii) evaluating the surface oxygen retention of doped- $\text{Li}_{1-x}\text{NiO}_2$ as compared to the pristine, un-doped state. The results of the screening process are presented together with an investigation and discussion of the dopant's impact on the local oxygen bonding environment and its relevance to macroscopic oxygen release. To validate the theoretical predictions, we choose Sb as the exemplary dopant and synthesize Sb-doped LiNiO_2 . We quantitatively determine Sb segregation behavior in Sb-doped LiNiO_2 and investigate its influence on electrochemical performance compared with pristine LiNiO_2 . Our proposed evaluation process is poised to resolve some longstanding challenges in fundamental doping effects on battery materials.

2 Methods

2.1 Computational details

All density functional theory (DFT) electronic structure calculations were performed using the Vienna *Ab initio* Simulation Package (VASP),^{43,44} with the Projector Augmented Wave (PAW) potentials.⁴⁵ The spin-polarized Generalized Gradient Approximation (GGA) parametrized by the Perdew–Burke–Ernzerhof (PBE)⁴⁶ employing the on-site Coulomb interaction approach (GGA+U) was used for the exchange–correlation functional with $U = 5.8$ and 6.2 eV for Ti 3d and Ni 3d orbitals, respectively.^{47,48} The cutoff energy for the plane wave expansion was set to 500 eV with a k -point density of 64 \AA^{-3} of reciprocal cell. All structures were optimized using a force convergence criterion of 0.03 eV \AA^{-1} and an electronic self-consistency convergence criterion of less than 10^{-6} eV . To determine the surface stability and the most dominant surface facet, we select six different surface facets: (104), (110), (100) for nonpolar surfaces and (003), (101), (012) for polar surfaces, based on previous theoretical and experimental studies.^{29,49,50} The nonpolar surfaces correspond to the type 1 surface according to Tasker's classification scheme⁵¹ with overall zero charge for each plane. The polar surfaces consist of a stacking sequence of charged planes with a nonzero net dipole moment. Thus, to avoid an artificial electric field across the slabs, we adopt the symmetric slab models with two identical surfaces. All slab structures were terminated by a 15 \AA vacuum interval to prevent spurious surface interactions resulting from the periodic boundary condition.

Surface stability. The surface stability was determined by calculating the surface energy (γ) of each facet using the following equation:

$$\gamma = \frac{E^{\text{slab}} - E^{\text{bulk}} + \sum_i (n_i^{\text{slab}} - n_i^{\text{bulk}})\mu_i}{2A} \quad (1)$$

where E^{slab} is the total energy of the slab structure with a given surface facet, E^{bulk} is the total energy of the corresponding



number of bulk LiNiO_2 cells, μ_i is the chemical potential of species i at the relative stoichiometry as compared to the bulk ($n_i^{\text{slab}} - n_i^{\text{bulk}}$) and A is the surface area. The nonpolar slabs satisfy the stoichiometry of bulk LiNiO_2 , so $n_i^{\text{slab}} - n_i^{\text{bulk}} = 0$ and γ is independent of μ_i values. For the polar slabs, there is excess or shortage of species i and γ is a function of μ_i . The allowed range of μ_{Li} , μ_{Ni} and μ_{O} are determined from the stable area of LiNiO_2 in the Li–Ni–O phase diagram (Fig. 1a). The chemical potentials μ_i are referenced to the corresponding elemental phases (*i.e.*, $\Delta\mu_i = \mu_i - E_i$, the elemental metal for Li and Ni, and an isolated O_2 molecule for O), and hence the equilibrium stability of LiNiO_2 is given by $\Delta\mu_{\text{Li}} + \Delta\mu_{\text{Ni}} + 2\Delta\mu_{\text{O}} = \Delta H_f(\text{LiNiO}_2)$, where $\Delta H_f(\text{LiNiO}_2)$ is the formation enthalpy of LiNiO_2 .

Dopant segregation. Two atomic sites are available for doping of LiNiO_2 , *i.e.*, the Ni- and Li-site. To determine the preferred dopant location, we calculate the doping formation energy difference ($\Delta E_f^{\text{Ni-Li}}$) between the two sites, using the equation:

$$\Delta E_f^{\text{Ni-Li}} = E_{\text{Ni}}^{\text{slab}} - E_{\text{Li}}^{\text{slab}} + \mu_{\text{Ni}} - \mu_{\text{Li}} \quad (2)$$

where the allowed range of μ_{Ni} and μ_{Li} are determined from the Li–Ni–O phase diagram and a typical LiNiO_2 synthetic environment at 600°C and $p(\text{O}_2) = 1 \text{ atm}$,⁵² *i.e.*, $\Delta\mu_{\text{O}} = -0.9 \text{ eV}$. The calculation of $\Delta\mu_{\text{O}}$ from temperature and pressure follows the methodology used in ref. 53 and is described in the ESI.† In addition, when a doping element is added during the synthesis process, it may occupy the surface region or the bulk region. To properly simulate and differentiate the surface and bulk regions, the distance between the surface and the bulk layer should be long enough to avoid any spurious interactions. Thus, to determine the dopant segregation behavior, we use a slab structure that contains a total of 9 layers (the surface is 8.3 Å apart from the bulk layer), then systematically substitute one Ni atom with one dopant in the i th layer, starting with the surface and subsequently moving the dopant to the center layer (5th) of the slab structure (see Fig. 2a). The total energy difference (ΔE) between the configuration of the dopant in the i th layer and in the center layer is calculated using the equation:

$$\Delta E = E_i^{\text{slab}} - E_c^{\text{slab}} \quad (3)$$

The configuration of the dopant in the center layer corresponds to a dilute dopant substituted in the bulk LiNiO_2 . Thus, ΔE captures the segregation preference, as a function of the dopant position in LiNiO_2 . To compare ΔE to competing thermodynamic drivers towards chemical homogeneity, we estimate the temperature, above which entropic effects dominate:

$$\Delta G = \Delta H - T\Delta S = \Delta H + TNk_{\text{B}}(x_{\text{M}} \ln x_{\text{M}} + x_{\text{Ni}} \ln x_{\text{Ni}}) = 0 \quad (4)$$

where ΔH is the dopant segregation enthalpy, T is the temperature, N is the total number of atoms in the slab structure, x_{M} and x_{Ni} are the mole fractions of the doping element and Ni. It should be noted that in the dopant segregation calculations, we performed non-spin-polarized GGA calculations to avoid spurious changes in magnetic states due to on-site electron localization.

Surface oxygen release energy. To study the surface oxygen evolution during delithiation of the pristine- and doped- LiNiO_2 , we choose the most stable surface facet from the surface stability analysis and generate the slab models for delithiated $\text{Li}_{1-x}\text{NiO}_2$. We adopt the ground-state structures of delithiated $\text{Li}_{1-x}\text{NiO}_2$ from the results of Arroyo y de Dompablo *et al.*^{54,55} The oxygen-deficient slab structure was constructed by removing one oxygen atom from both surface planes. Thus, the oxygen release energy (E_f^{Vo}) for a given slab model is defined as:

$$E_f^{\text{Vo}} = \frac{1}{2}(E_{\text{Vo}}^{\text{slab}} - E_{\text{P}}^{\text{slab}} + 2\mu_{\text{O}}) \quad (5)$$

where $E_{\text{Vo}}^{\text{slab}}$ and $E_{\text{P}}^{\text{slab}}$ are the total energies of the oxygen-deficient and pristine slab structure, respectively. An equilibrium μ_{O} was determined at conditions relevant for the electrochemical testing environment of 30°C and $p(\text{O}_2) = 0.2 \text{ atm}$, resulting in $\mu_{\text{O}} = -5.2 \text{ eV}$ (see ESI for more details†). The overestimated O_2 binding energy in DFT was corrected, using

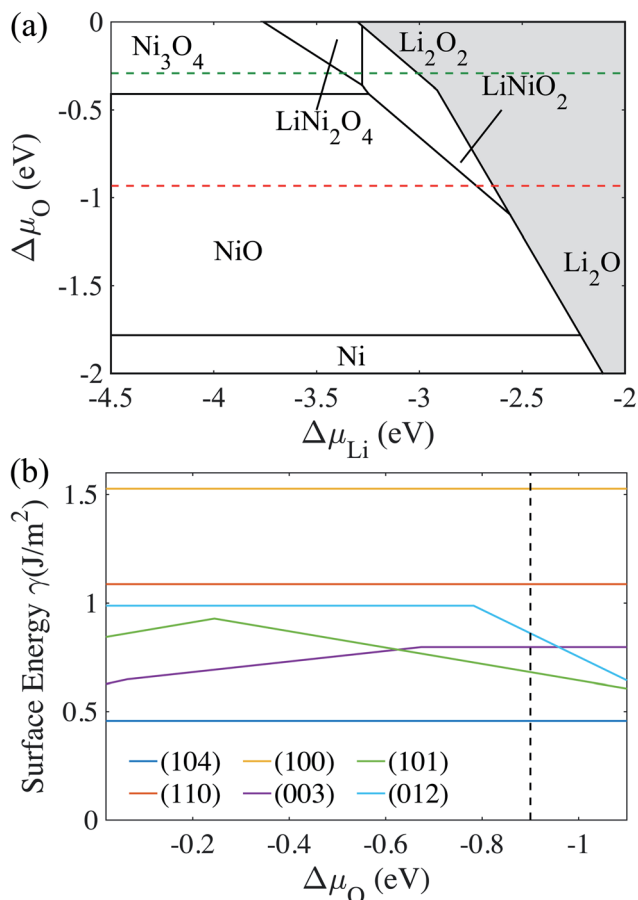


Fig. 1 (a) Phase diagram of Li–Ni–O system as a function of changes in Li and O chemical potentials showing the stability region of bulk LiNiO_2 . The red dashed line represents a synthesis environment at 600°C and $p(\text{O}_2) = 1 \text{ atm}$. The green dashed line represents an electrochemical testing environment at 30°C and $p(\text{O}_2) = 0.2 \text{ atm}$. (b) Surface energy of LiNiO_2 of six low-index surfaces as a function of oxygen chemical potential. The black dashed line corresponds to $\Delta\mu_{\text{O}}$ at 600°C and $p(\text{O}_2) = 1 \text{ atm}$.



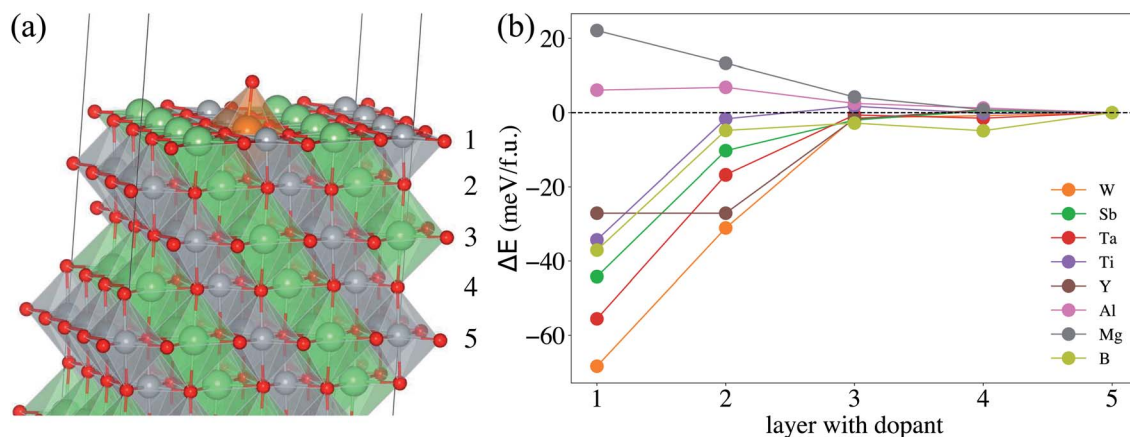


Fig. 2 (a) A slab model of a doped-LiNiO₂ (104) facet. The orange atom represents the doping element and substitutes one Ni atom in the 1st, 2nd, 3rd, 4th, and 5th layer. An oxygen atom is added on the 1st layer (color code: green for Li atom, grey for Ni atom, red for O atom and orange for dopant). (b) The total energy difference (ΔE) between the dopant in the i th layer and 5th layer as a function of the dopant position in doped-LiNiO₂.

the methodology of Wang *et al.*⁵⁶ A site-averaged E_f^{Vo} was derived with an associated standard deviation over all symmetrically unique oxygen vacancy sites. For the doped-Li_{1-x}NiO₂ slab structures, we substitute one Ni at the surface with the doping element and follow the same procedure to calculate $E_f^{Vo}(\text{doped})$. Therefore, the relative oxygen release energy, $\Delta E_f^{Vo} = E_f^{Vo}(\text{doped}) - E_f^{Vo}(\text{pristine})$, provides a metric of the oxygen retention capability of a considered doping element.

Bond strength. To investigate the nature of the chemical bonding between doping element and oxygen, we perform projected crystal orbital Hamiltonian population (pCOHP) analysis on the electronic wavefunctions using the LOBSTER codes.⁵⁷ The integration of pCOHP (ICOHP) up to the Fermi level yields a measure of the dopant–oxygen bond hybridization,^{58,59} which is used to analyze and correlate oxygen loss with local bonding environments and electronic features.

2.2 Experimental details

TEM experiments. The TEM imaging and chemical analysis were carried out on a FEI Talos F200X transmission electron microscope with an X-FEG field emission source operated at 200 keV. High-angle annular dark-field transmission electron microscopy (HAADF STEM) mode was used to acquire the atomic-resolution Z contrast images. Elemental dispersive spectroscopy (EDS) experiments were performed in HAADF STEM mode with super-X EDS system integrated into the Talos F200X TEM.

Material synthesis. The LiNiO₂ and Sb-doped LiNiO₂ were synthesized through a simple co-precipitation method followed by a high temperature calcination. The starting solution (40 mL of NaOH and NH₃·H₂O aqueous solution with a molar ratio NH₃/NaOH = 1.25, pH value was adjusted to 11.0), and the base solution (100 mL of NaOH and NH₃·H₂O aqueous solution with a molar ratio NH₃/NaOH = 1.25) were prepared first.

LiNiO₂. We prepared the transition metal solution using 0.1 mol NiSO₄·6H₂O dissolved in 100 mL DI water. The base

solution and the transition metal solution were simultaneously pumped into the starting solution at a rate around 2 mL min⁻¹ with the continuous stir at 55 °C under N₂ protection. The pH value in the reaction solution was maintained around 11.0 ± 0.2 by carefully tuning the pumping rate of base solution. The precipitate (*i.e.*, hydroxide precursor) was aged for three hours, collected, washed, and filtered with DI water and IPA. Then, the hydroxide precursor was obtained after dried in vacuum oven overnight at 105 °C. Finally, we thoroughly mixed LiOH with the hydroxide precursor at the ratio of 1 : 1 and calcined it at 460 °C for 2 h and then at 675 °C for 6 h with oxygen following (1 L min⁻¹) to obtain the final product.

Sb-doped LiNiO₂ (2% Sb). We first prepared the transition metal solution using 0.098 mol NiSO₄·6H₂O dissolved in 100 mL DI water. The base solution and the transition metal solution were simultaneously pumped into the starting solution at a rate around 2 mL min⁻¹ with continuous stirring at 55 °C under N₂ protection. The pH value in the reaction solution was maintained around 11.0 ± 0.2 by carefully tuning the pumping rate of the base solution. The SbCl₃ powder (0.002 mol) was poured into the reaction after the transition metal solution was ran out. The precipitate (*i.e.*, hydroxide precursor) was aged for three hours, collected, washed, and filtered with DI water and IPA. Then, the hydroxide precursor was obtained after dried in vacuum oven overnight at 105 °C. Finally, we thoroughly mixed LiOH with the hydroxide precursor at the ratio of 1 : 1.06 and calcined it at 460 °C for 2 h and then at 675 °C for 6 h with oxygen following (1 L min⁻¹) to obtain the final product.

Sb-doped LiNiO₂ (1% Sb). The synthesis protocol was the same as the Sb-doped LiNiO₂ (2% Sb), except for the use of 0.099 mol NiSO₄·6H₂O for the transition metal solution and 0.001 mol SbCl₃ powder.

Electrochemical characterization. The active material of 90%, carbon black of 5%, and 5% PVdF (polyvinylidene fluoride) dissolved in NMP were thoroughly mixed to form a slurry. The slurry was cast on to carbon-coated Al foils by a doctor blade. The electrodes were then punched into disks (diameter =



10 mm) and dried overnight in a vacuum oven at 120 °C and transferred into an Ar filled glove box. The CR2032 coin cells were assembled using the cathode, lithium metal as the anode, 1.0 M LiPF₆ dissolved in EC and EMC (3 : 7 in weight plus 2% VC as the additive) as the electrolyte, and Whatman glass fibers as the separator. The coin cells were evaluated on a Wuhan LANHE battery testing system at room temperature (23 °C).

3 Results and discussion

3.1 Computational prediction

To determine the chemical potential limits of bulk LiNiO₂ stability, we use formation energies from the Materials Project database, as of January 2019.⁴⁸ Fig. 1a shows the as-obtained phase diagram of Li–Ni–O as a function of the chemical potentials of lithium μ_{Li} and oxygen μ_{O} , where Li metal (E_{Li}) is chosen as reference state and hence $\Delta\mu_{\text{Li}} = \mu_{\text{Li}} - E_{\text{Li}}$, and $\Delta\mu_{\text{Li}}$ is directly proportional to the Li|Li⁺ voltage. $\Delta\mu_{\text{O}}$ is a function of pressure and temperature. The red dashed line at $\Delta\mu_{\text{O}} = -0.93$ eV in Fig. 1a represents an equilibrium synthesis environment of LiNiO₂ at 600 °C and $p(\text{O}_2) = 1$ atm (ref. 52) and the green dashed line at $\Delta\mu_{\text{O}} = -0.29$ eV represents an electrochemical testing environment at 30 °C and $p(\text{O}_2) = 0.2$ atm. Hence we can approximate synthesis and electrochemical testing conditions in terms of $\Delta\mu_{\text{O}}$. The methodology of the $\Delta\mu_{\text{O}}$ calculation from temperature and pressure is described in the ESI.† As illustrated in Fig. 1a, the LiNiO₂ phase is found to be thermodynamically stable for $-1.10 < \Delta\mu_{\text{O}} < -0.02$ eV, $-3.28 < \Delta\mu_{\text{Li}} < -2.56$ eV. Under oxidizing conditions, the conversion to the spinel Ni₃O₄ and cation-mixed spinel LiNi₂O₄ defines the lower limit of $\Delta\mu_{\text{Li}}$ (upper limit voltage against Li/Li⁺). Overlithiation results in the formation of Li₂O in reducing environments and Li₂O₂ under oxidizing conditions, defining the upper limit of $\Delta\mu_{\text{Li}}$ (lower limit voltage against Li/Li⁺).

We determine the majority surface(s) of LiNiO₂ by exploring different surface facets and their respective surface energies (γ), as a function of termination. Fig. 1b shows the calculated γ represented as the lowest energy for six surface facets as a function of $\Delta\mu_{\text{O}}$, where the relevant range of $\Delta\mu_{\text{O}}$ is obtained from the stability range of LiNiO₂ (see Fig. 1a). We find that the (104) facet exhibits the lowest γ for the entire range of $\Delta\mu_{\text{O}}$, thus presents – by far – the most stable surface facet, which is in agreement with previous studies.^{29,49} The black dashed line in Fig. 1b corresponds to an equilibrium synthesis environment of LiNiO₂ with (104) as the dominant surface facet. Therefore, in the following slab models and surface dopant investigation, we choose (104) surface facet to represent the Li_{1-x}NiO₂ surface chemistry and structure.

To determine the preferable surface dopant location in LiNiO₂, as a function of dopant species, we calculate the doping formation energy difference ($\Delta E_{\text{f}}^{\text{Ni-Li}}$) between doping at the surface Ni- vs. the surface Li-site. Fig. S2a† shows that for all the considered dopants, $\Delta E_{\text{f}}^{\text{Ni-Li}}$ is negative for the entire range of $\Delta\mu_{\text{Li}}$, which implies that the candidate doping elements prefer to occupy the Ni-site. The occupations of Ni sites by Sb, Ti, Al and Mg in LiNiO₂ also agree well with the experimental results.^{33,60,61} Graphing $\Delta E_{\text{f}}^{\text{Ni-Li}}$ of each dopant against its

corresponding ionic radius (see Fig. S2b†) clearly shows that a dopant with ionic radius similar to that of Ni³⁺ tends to exhibit more negative $\Delta E_{\text{f}}^{\text{Ni-Li}}$ and hence more favorably occupy the Ni-site. Next, we analyze the dopant segregation behavior in doped-LiNiO₂ by calculating the total energy difference (ΔE) between the configurations of the dopant in the *i*th layer and in the center layer (see Fig. 2b). We find that W, Sb, Ta, Ti, Y, and B exhibit a strong tendency to segregate to the surface region, while Mg prefers to reside in the bulk. In addition, as observed in Fig. 2b, ΔE quickly converges to zero for all the dopants as a function of distance from the surface, which indicates that our models properly differentiate between the surface and bulk regions.

Using eqn (4) we estimate the lowest $|\Delta E|$ that overcomes the entropic term towards chemical homogeneity. LiNiO₂ synthesis temperature is around 600 °C,⁵² which corresponds to $|\Delta E| = \Delta H = 7$ meV per f.u. This implies that $|\Delta E|$ should be higher than 7 meV per f.u. to ensure that dopant surface segregation is thermodynamically driven at the relevant synthesis temperature. For example, a surface segregation energy of 20 meV per f.u. requires a synthesis temperature over 2500 K to thermodynamically drive homogeneous distribution. Therefore, we conclude that $|\Delta E|$ is sufficient to drive surface dopant segregation behavior for W, Sb, Ta, Ti, Y, and B. Mg and Al both prefer the bulk but Al exhibits such a weak preference that we expect Al to uniformly distribute at relevant synthesis temperatures. Weigel *et al.* reported that in cation-doped Ni-rich NCM cathodes, the layer near the surface tends to be slightly richer in dopants than that of the bulk,⁶² which corresponds well with the segregation phenomena of most of our considered dopants. Moreover, in Mg/Ti co-doped LiNiO₂, Ti exhibits a surface enrichment, whereas Mg distributes homogeneously.⁶⁰ Our calculations provide thermodynamic rationale for the observed homogeneous bulk Mg distribution. Furthermore, previous experimental work also supports the expectation of homogeneous distribution of Al doping in LiNiO₂.⁶³

After identifying (104) as the most stable surface facet, the Ni-site as the preferable dopant location and relevant dopant segregation behaviors, we examine the correlation between surface oxygen evolution and state of charge by incrementally removing Li from pristine- and doped-LiNiO₂. Fig. S3† depicts the delithiated Li_{1-x}NiO₂ slab structures with (104) surface facet, following the most stable Li decorations in bulk Li_{1-x}NiO₂ as obtained in ref. 55. The oxygen release energy ($E_{\text{f}}^{\text{V}0}$) at each delithiated state was calculated following eqn (5) as described in Section 2 and is presented in Fig. 3a. As expected from previous work,⁴² $E_{\text{f}}^{\text{V}0}$ decreases rapidly upon delithiation: for fully lithiated LiNiO₂, the averaged $E_{\text{f}}^{\text{V}0}$ is 1.27 eV; when 75% Li is deintercalated, the averaged $E_{\text{f}}^{\text{V}0}$ becomes 0.15 eV, *i.e.*, oxygen release becomes much more favorable at high charge state. Moreover, oxygen evolution is further enhanced at higher temperatures and higher states of charge (*e.g.*, $x \geq 0.75$).^{64–66} It is worth pointing out that the calculated oxygen release energy presented here is based on an air environment, with $T = 30$ °C and $p(\text{O}_2) = 0.2$ atm. At an elevated temperature of 200 °C, the averaged $E_{\text{f}}^{\text{V}0}$ reduces to -0.05 eV, *i.e.*, oxygen is predicted to spontaneously release from the surface for pristine Li_{0.25}NiO₂



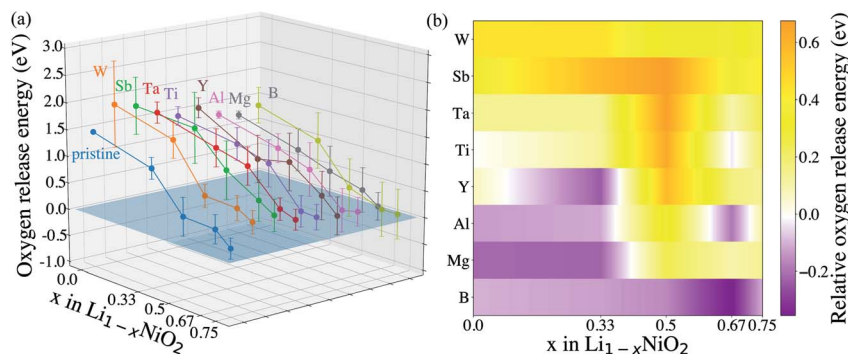


Fig. 3 (a) Oxygen release energy as a function of Li content of the pristine- and doped- LiNiO_2 , based on an air environment, with $T = 30^\circ\text{C}$ and $p(\text{O}_2) = 0.2$ atm. (b) The relative surface oxygen release energies of doped LiNiO_2 with respect to the pristine phase. An orange color indicates an improved oxygen retention, while a purple color indicates a reduced oxygen retention as compared to the pristine phase.

and lower Li contents. This is consistent with the observed oxygen evolution related weight loss as measured by thermogravimetry around 200°C in $\text{Li}_{1-x}\text{NiO}_2$ ($x \geq 0.8$).⁶⁴

To analyze the impact of surface dopants in $\text{Li}_{1-x}\text{NiO}_2$, we compare E_f^{Vo} for doped- LiNiO_2 with that of the pristine, undoped material. Fig. 3 shows that W, Sb, Ta and Ti effectively increase E_f^{Vo} as compared to pristine- $\text{Li}_{1-x}\text{NiO}_2$. For example, at 75% Li extraction, the averaged E_f^{Vo} of W-, Sb-, Ta- and Ti-doped $\text{Li}_{0.25}\text{NiO}_2$ are 0.53, 0.56, 0.40 and 0.35 eV, respectively. On the other hand, the averaged E_f^{Vo} of surface B-doped $\text{Li}_{0.25}\text{NiO}_2$ is calculated at 0.05 eV, which indicates that surface boron actually stimulates surface oxygen evolution and therefore is expected to deteriorate the thermal stability of $\text{Li}_{1-x}\text{NiO}_2$, as related to surface oxygen loss. To better illustrate the dopant effectiveness against surface oxygen loss, we calculate the relative oxygen release energy (ΔE_f^{Vo}) following the procedure in Section 2. Fig. 3b shows that W-, Sb-, Ta- and Ti-doped $\text{Li}_{1-x}\text{NiO}_2$ exhibit higher E_f^{Vo} values than pristine- $\text{Li}_{1-x}\text{NiO}_2$ for all Li content (e.g. states of charge), which implies that W, Sb, Ta, and Ti are all expected to enhance surface oxygen retention of $\text{Li}_{1-x}\text{NiO}_2$, with W and Sb are predicted to be the most promising dopants. Interestingly, Ta was recently theoretically predicted and experimentally validated to alleviate oxygen evolution from Li-excess, Mn-rich layered cathode materials.⁴² In addition, Ti has been found to improve the oxygen stability at the surface of Ti-doped $\text{LiNi}_{0.8}\text{Mn}_{0.1}\text{Co}_{0.1}\text{O}_2$ and improve its electrochemical performance.³⁴

Finally, we attempt to elucidate the chemical and structural features that give rise to these dopants' effectiveness (or lack thereof) towards mitigating surface oxygen loss. In this context, a common misconception is to equate a bulk Gibbs free energy of oxide formation with the ability to limit oxygen loss. For example, it is often thought that Al_2O_3 would strongly retain oxygen because the Gibbs free energy of the oxidation reaction $\text{Al} + \text{O}_2 \rightarrow \text{Al}_2\text{O}_3$ is one of the lowest found in the Ellingham diagrams.⁶⁷ However, the Al oxidation reaction is not just a measure of the cohesive energy between Al^{3+} and O^{2-} in the corundum structure; its main contribution is the actual oxidation, e.g. that Al is an extremely electropositive metal. In Li-ion cathodes, Al (and similarly electropositive elements) stay

firmly oxidized, and hence this contribution is not relevant. Similarly, we do not expect any global structural features (e.g. the cohesive energy of the corundum structure) to play a significant role here, as the dopant and the oxygen are not arranged in their preferred long-range structural arrangement. Hence, we turn to local chemical descriptors such as the chemical bonding between the dopant and the oxygen and perform a quantitative calculation of the bond strength. Fig. 4 shows the calculated projected crystal orbital Hamiltonian population (pCOHP) plots for Sb-O, Ta-O, Ti-O and B-O interactions for doped LiNiO_2 , which are averaged over all the surface dopant-oxygen contacts up to 3.0 \AA in length. Bonding (stabilizing) contributions to the electronic band structure are represented by positive pCOHP, whereas antibonding ones are represented by negative pCOHP. From the pCOHP illustrated in Fig. 4 we find that Sb-O, Ta-O and Ti-O interactions are mostly bonding while the B-O bonding is characterized by massive antibonding interactions. Thus, the bond strength of Sb-O, Ta-O and Ti-O pairs are interpreted as significantly stronger than that of B-O. To obtain a more quantitative estimate of the bond strength, we integrate pCOHP (ICOHP) over the relevant energy range of -20 eV to 0 . Fig. 5a shows the variance of ICOHP as a function of doping elements, along with their corresponding averaged E_f^{Vo} values of fully lithiated LiNiO_2 . We find a clear correlation between higher E_f^{Vo} and a larger -ICOHP value, which implies that a stronger dopant-oxygen bond leads to a better surface oxygen retention. Fig. 5a also illustrates a dopant with a higher oxidation state, such as W^{6+} , generally exhibit stronger dopant-oxygen bond (higher -ICOHP) and better oxygen retention ability (higher E_f^{Vo}) than dopants of lower oxidation states, such as Mg^{2+} . This trend can be rationalized by the change of electrostatic interaction between dopant and oxygen, as W^{6+} is expected to exhibit a stronger electrostatic interaction with oxygen. Similarly, we expect other dopants with high oxidation states, such as Mo^{6+} and Nb^{5+} , as promising candidates for alleviating surface oxygen loss from LiNiO_2 . Indeed, both Mo^{6+} and Nb^{5+} have been confirmed to form a strong dopant-oxygen bond and reduce oxygen evolution in Li-rich layered cathode materials.^{68,69} Further insight into the nature of the dopant-oxygen bonding is



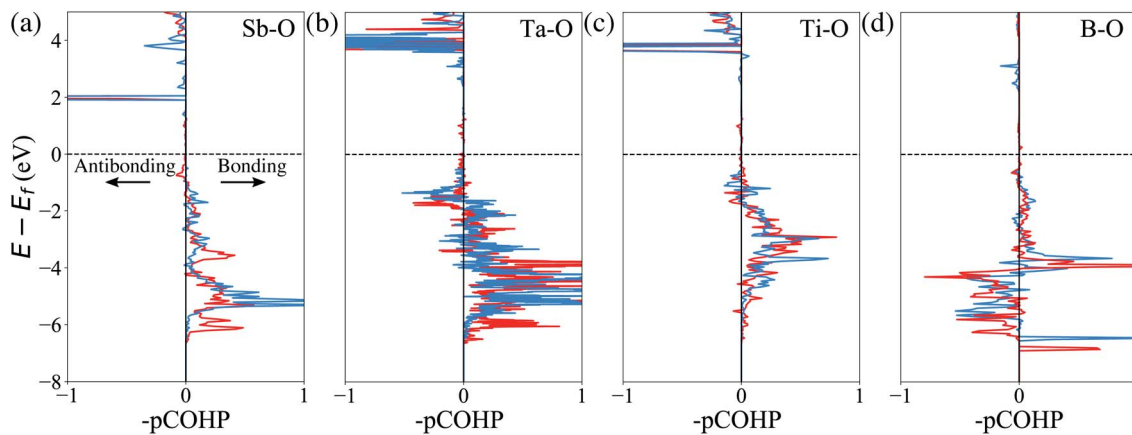


Fig. 4 Calculated pCOHP of (a) Sb–O, (b) Ta–O, (c) Ti–O, and (d) B–O chemical bonds as reconstructed from electronic wavefunctions. A horizontal dashed line represents the Fermi level E_f , which is set to the valence band maximum (VBM). Blue and red curves represent spin-up and spin-down, respectively.

provided by an electron localization function (ELF) analysis, as shown in Fig. 5b. The green regions between the Sb and O atoms correspond to shared electrons, which signifies strong electron hybridization and increased covalency. On the other hand, the Mg-doped surface layer displays weak hybridization and covalency between the Mg and oxygen ions. Furthermore, Sb^{5+} exhibits a stronger electrostatic bond with oxygen as compared with the lower-valent Mg^{2+} . Therefore, a higher valence, as well as a higher degree of electrons sharing and covalency between Sb and O leads to a stronger Sb–O bond and mitigation of the surface oxygen evolution. Similar oxygen retention due to electron hybridization was also reported in Os-doped Li_2MnO_3 structures.⁴²

To summarize, we rationalize the effectiveness of W, Sb, Ta, and Ti to enhance surface oxygen retention of $\text{Li}_{1-x}\text{NiO}_2$, which is attributed to their stronger local bonding interactions with oxygen, as compared to the pristine Ni–O pair. Conversely, Al and Mg were not found to improve oxygen retention, while B was expected to deteriorate the surface oxygen loss in $\text{Li}_{1-x}\text{NiO}_2$. From a broader perspective, bonding descriptors based on the local oxygen chemical and structural environment are found to capture the ability to mitigate surface oxygen loss. Interestingly, similar conclusions were recently presented for two Na-ion cathodes, where local surface undercoordination due to different cation distributions resulted in different oxygen loss characteristics.⁷⁰

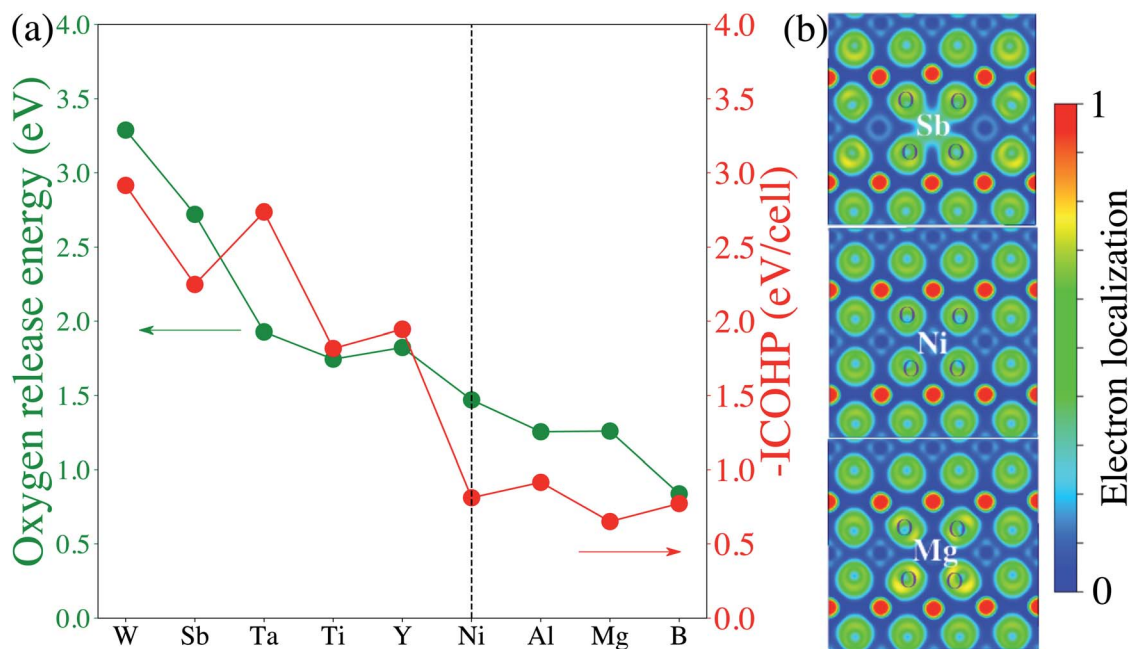


Fig. 5 (a) Averaged oxygen release energy of pristine- and doped- LiNiO_2 and $-\text{ICOHP}$ values of dopant–oxygen pairs as a function of doping elements. The calculation is based on fully lithiated LiNiO_2 . The perpendicular dashed line represents the values for pristine LiNiO_2 . (b) 2D electron localization function contour plots for the surface slices of Sb-, pristine-, and Mg-doped LiNiO_2 .



3.2 Experimental validation

Among the four recommended dopants, we choose Sb as an exemplary dopant and validate our theoretical predictions by experimental synthesis, structural characterization and electrochemical tests. We synthesize pristine LiNiO_2 and Sb-doped LiNiO_2 through a simple co-precipitation method (see Section 2). The inductively coupled plasma mass spectrometry (ICP-MS) confirm that the dopant concentrations are in good agreement with the desired compositions (1% and 2% in the atomic ratio). Fig. 6a presents an atomic resolution HAADF STEM image of 2% Sb-doped LiNiO_2 obtained along $[100]$ zone axis. The results show that the Sb-doped LiNiO_2 has a perfect layered structure (space group $R\bar{3}m$) with alternating transition metal layer and Li layer. EDS maps and quantitative analysis (see Fig. 6b and S3†) show that Sb is inclined to enrich to the particle surface with an

average content of ~ 4.5 at%, while it has a relatively uniform distribution in the bulk with an average content of 3.3 at%. The surface enrichment of Sb confirms the theoretical prediction of Sb segregation behavior in Fig. 2. In addition, it should be noted that there is a discrepancy between the Sb concentration obtained from ICP-MS and the value given by EDS measurement. We attribute the difference to the following two factors: (1) our EDS system's energy axis is slightly off calibration, which could give rise to the difference. (2) We also acknowledge there could be composition inhomogeneity from particle to particle. However, the discrepancy doesn't affect the conclusion that Sb has a higher concentration in the particle surface.

The electrochemical performance of the pristine and Sb-doped LiNiO_2 are evaluated in galvanostatic mode, see Fig. 6c and d. Dopants usually decrease the reversible capacity of the

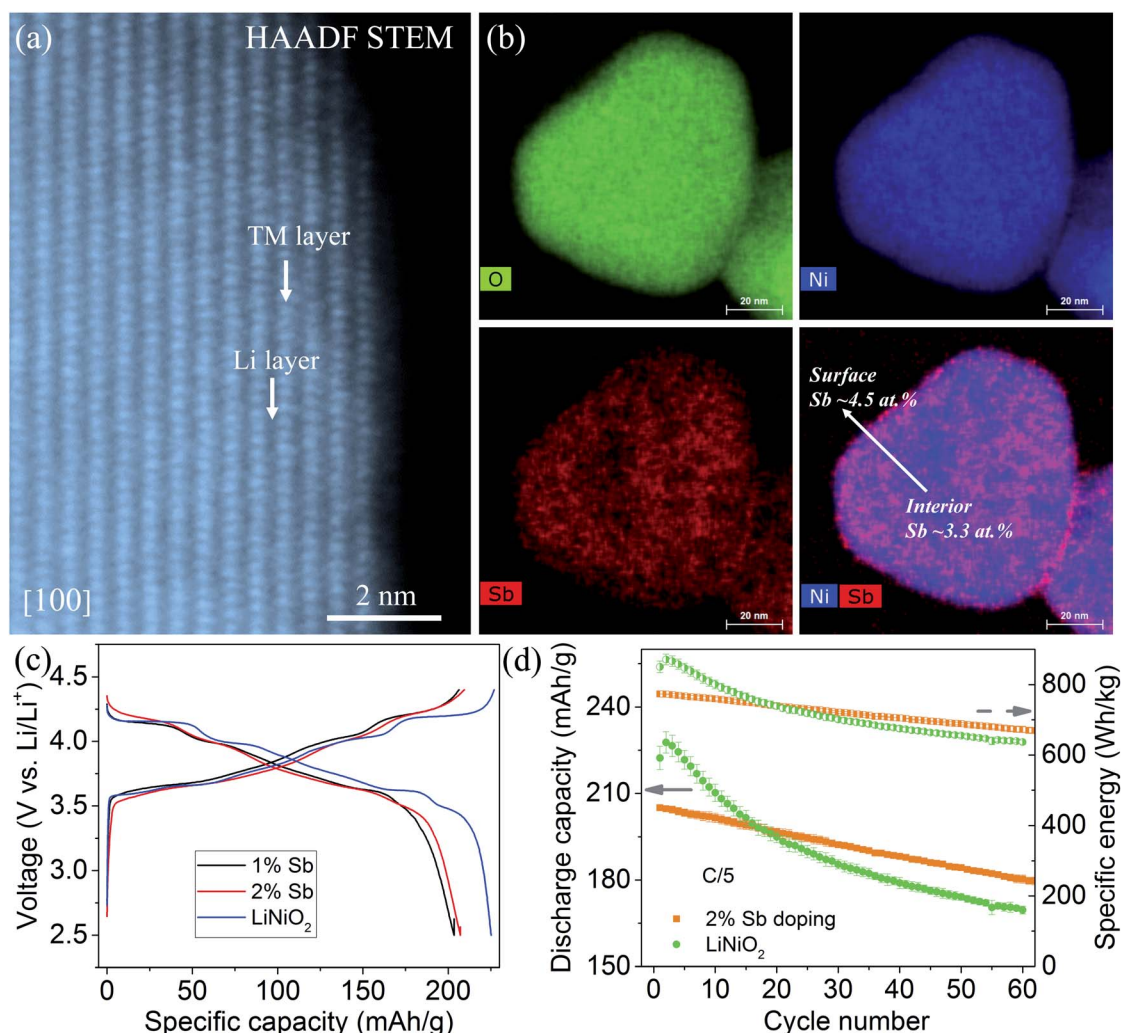


Fig. 6 (a) Atomic resolution high-angle annular dark-field transmission electron microscopy (HAADF STEM) image of a 2% Sb-doped LiNiO_2 along $[100]$ zone axis. The transition metal (TM) layer and Li layer are indicated in the $R\bar{3}m$ lattice. (b) EDS maps of O, Ni, Sb as well as the overlapped map of Sb and Ni of typical Sb-doped LiNiO_2 primary particle. Surface segregation of Sb is identified as the average ratio of Sb/(Sb + Ni) increased from 3.3 to 4.5 at% from the interior to the surface. (c) Second charge profiles of the cells containing the cathodes of LiNiO_2 , 1% Sb-doped LiNiO_2 , and 2% Sb-doped LiNiO_2 at C/10 within 2.5–4.4 V vs. Li/Li^+ . (d) Discharge capacity and specific energy as a function of the cycle number of the cells containing the cathodes of LiNiO_2 and 2% Sb-doped LiNiO_2 at C/5 within 2.5–4.4 V vs. Li/Li^+ . The error bars in (d) are created based on the repeated measurements.



LiNiO₂ cathode because of a lower nickel concentration.^{60,61,71} The reversible capacity of ~200 mA h g⁻¹ both for the 1% and 2% Sb-doped LiNiO₂ is slightly lower than that of the pure LiNiO₂ of ~225 mA h g⁻¹ at C/10 within 2.5–4.4 V vs. Li/Li⁺ (see Fig. 6c). By comparing the charge/discharge profiles, the 2% Sb-doped LiNiO₂ delivers slightly smoother curves. It is well accepted that many dopants inhibit the multiple phase transformations, resulting in less step-like voltage profiles.^{60,71–73} In addition, the 2% Sb-doped LiNiO₂ shows the capacity and energy retention of ~87.8% and 86.6% after 60 cycles at C/5, respectively (see Fig. 6d). On the other hand, pristine LiNiO₂ has retention of 74.7% and 76.6% for discharge capacity and specific energy after 60 cycles, respectively, although it displays the higher initial values of both. We believe there is still a large space to improve the electrochemical performance of Sb-doped LiNiO₂ through optimizing the synthesis conditions. The improved electrochemical performance of Sb-doped LiNiO₂ is expected from our theoretical prediction and may be attributed to the mitigated surface oxygen loss as a result of Sb doping.

4 Conclusions

Using first-principles calculations, we systematically evaluate the effectiveness of a select set of doping elements to enhance surface oxygen retention of Li_{1-x}NiO₂. Based on dopants that have been previously proposed to improve the cycling performance of Ni-rich layered oxide cathode materials, we choose eight candidates: W⁶⁺, Sb⁵⁺, Ta⁵⁺, Ti⁴⁺, Y³⁺, Al³⁺, B³⁺ and Mg²⁺. The evaluation process includes choosing the most stable surface facet from surface stability analysis of LiNiO₂, determining the preferable atomic site and segregation behavior for each dopant, and evaluating the surface oxygen retention of doped-Li_{1-x}NiO₂ as compared to the pristine material. The following observations and conclusions are made:

(1) All considered dopants preferably locate at the Ni-site in fully lithiated LiNiO₂. W, Sb, Ta, Ti, Y and B exhibit a strong tendency to segregate to the surface region, while Mg prefers to reside in the bulk. Al tends to uniformly distribute from the surface to the bulk.

(2) Bonding descriptors based on the local oxygen chemical and structural environment, such as degree of electron hybridization, are found to correlate strongly with surface oxygen retention.

(3) W, Sb, Ta, and Ti are identified as the most promising dopants to mitigate surface oxygen evolution of Li_{1-x}NiO₂, and all four cations were found to display a higher degree of electron hybridization between the dopant and oxygen, as compared to the pristine Ni–O bond.

Finally, we explore Sb as an exemplary dopant and synthesize Sb-doped LiNiO₂ to validate our theoretical predictions. We found that 2% Sb-doped LiNiO₂ indeed exhibits a surface enrichment of Sb and improved electrochemical performance, as compared with pristine LiNiO₂. Hence, inclusion of Sb to mitigate oxygen evolution in high-voltage, particularly Ni-rich layered cathodes is a promising direction warranting further exploration. Our work also highlights the effectiveness of

a collaborated *in silico* and experimental approach in material design and discovery.

Conflicts of interest

There are no conflicts to declare.

Acknowledgements

This work was supported by the U.S. Department of Energy's Office of Energy Efficiency and Renewable Energy (EERE) under the Award Number: DE-EE0008444. The research was performed using computational resources sponsored by the Department of Energy's Office of Energy Efficiency and Renewable Energy and located at the National Renewable Energy Laboratory.

Notes and references

- 1 N. Nitta, F. Wu, J. T. Lee and G. Yushin, *Mater. Today*, 2015, **18**, 252–264.
- 2 Q. Liu, X. Su, D. Lei, Y. Qin, J. Wen, F. Guo, Y. A. Wu, Y. Rong, R. Kou, X. Xiao, F. Aguesse, J. Bareño, Y. Ren, W. Lu and Y. Li, *Nat. Energy*, 2018, **3**, 936–943.
- 3 E. A. Olivetti, G. Ceder, G. G. Gaustad and X. Fu, Lithium-Ion Battery Supply Chain Considerations: Analysis of Potential Bottlenecks in Critical Metals, *Joule*, 2017, **1**, 229–243.
- 4 S.-T. Myung, F. Maglia, K.-J. Park, C. S. Yoon, P. Lamp, S.-J. Kim and Y.-K. Sun, *ACS Energy Lett.*, 2017, **2**, 196–223.
- 5 D. Andre, S. J. Kim, P. Lamp, S. F. Lux, F. Maglia, O. Paschos and B. Stiaszny, Future generations of cathode materials: an automotive industry perspective, *J. Mater. Chem. A*, 2015, **3**, 6709–6732.
- 6 H.-J. Noh, S. Yoon, C. S. Yoon and Y.-K. Sun, *J. Power Sources*, 2013, **233**, 121–130.
- 7 J. H. Kim, H. H. Ryu, S. J. Kim, C. S. Yoon and Y. K. Sun, *ACS Appl. Mater. Interfaces*, 2019, **11**, 30936–30942.
- 8 C. Delmas, J. P. Pérès, A. Rougier, A. Demourgues, F. Weill, A. Chadwick, M. Broussely, F. Pertion, P. Biensan and P. Willmann, *J. Power Sources*, 1997, **68**, 120–125.
- 9 H. Arai, S. Okada, H. Ohtsuka, M. Ichimura and J. Yamaki, *Solid State Ionics*, 1995, **80**, 261–269.
- 10 W. Li, J. N. Reimers and J. R. Dahn, *Solid State Ionics*, 1993, **67**, 123–130.
- 11 H. Li, N. Zhang, J. Li and J. R. Dahn, *J. Electrochem. Soc.*, 2018, **165**, A2985–A2993.
- 12 C. S. Yoon, D.-W. Jun, S.-T. Myung and Y.-K. Sun, *ACS Energy Lett.*, 2017, **2**, 1150–1155.
- 13 K. Edström, T. Gustafsson and J. O. Thomas, *Electrochim. Acta*, 2004, **50**, 397–403.
- 14 D. H. Jang and S. M. Oh, *J. Electrochem. Soc.*, 1997, **144**, 3342–3348.
- 15 S.-K. Jung, H. Gwon, J. Hong, K.-Y. Park, D.-H. Seo, H. Kim, J. Hyun, W. Yang and K. Kang, *Adv. Energy Mater.*, 2014, **4**, 1300787.



- 16 P. Yan, J. Zheng, Z. K. Tang, A. Devaraj, G. Chen, K. Amine, J. G. Zhang, L. M. Liu and C. Wang, *Nat. Nanotechnol.*, 2019, **14**, 602–608.
- 17 E. Hu, X. Yu, R. Lin, X. Bi, J. Lu, S. Bak, K. W. Nam, H. L. Xin, C. Jaye, D. A. Fischer, K. Amine and X. Q. Yang, *Nat. Energy*, 2018, **3**, 690–698.
- 18 S. Hwang, W. Chang, S. M. Kim, D. Su, D. H. Kim, J. Y. Lee, K. Y. Chung and E. A. Stach, *Chem. Mater.*, 2014, **26**, 1084–1092.
- 19 S. Sharifi-Asl, J. Lu, K. Amine and R. Shahbazian-Yassar, *Adv. Energy Mater.*, 2019, **9**, 1900551.
- 20 J. Cheng, E. Sivonxay and K. A. Persson, *ACS Appl. Mater. Interfaces*, 2020, **12**, 35748–35756.
- 21 H. Xie, K. Du, G. Hu, Z. Peng and Y. Cao, *J. Phys. Chem. C*, 2016, **120**, 3235–3241.
- 22 Z. Yang, X. Guo, W. Xiang, W. Hua, J. Zhang, F. He, K. Wang, Y. Xiao and B. Zhong, *J. Alloys Compd.*, 2017, **699**, 358–365.
- 23 Z. Zhang, D. Chen and C. Chang, *RSC Adv.*, 2017, **7**, 51721–51728.
- 24 C. Poullierie, L. Croguennec, P. Biensan, P. Willmann and C. Delmas, *J. Electrochem. Soc.*, 2000, **147**, 2061–2069.
- 25 M. Zhang, H. Zhao, M. Tan, J. Liu, Y. Hu, S. Liu, X. Shu, H. Li, Q. Ran, J. Cai and X. Liu, *J. Alloys Compd.*, 2019, **774**, 82–92.
- 26 T. Ohzuku, A. Ueda and M. Kouguchi, *J. Electrochem. Soc.*, 1995, **142**, 4033–4039.
- 27 D. Wang, X. Li, Z. Wang, H. Guo, Y. Xu, Y. Fan and J. Ru, *Electrochim. Acta*, 2016, **188**, 48–56.
- 28 Y. Nishida, K. Nakane and T. Satoh, *J. Power Sources*, 1997, **68**, 561–564.
- 29 K.-J. Park, H.-G. Jung, L.-Y. Kuo, P. Kaghazchi, C. S. Yoon and Y.-K. Sun, *Adv. Energy Mater.*, 2018, **8**, 1801202.
- 30 R. Du, Y. Bi, W. Yang, Z. Peng, M. Liu, Y. Liu, B. Wu, B. Yang, F. Ding and D. Wang, *Ceram. Int.*, 2015, **41**, 7133–7139.
- 31 H. Zhu, T. Xie, Z. Chen, L. Li, M. Xu, W. Wang, Y. Lai and J. Li, *Electrochim. Acta*, 2014, **135**, 77–85.
- 32 U. H. Kim, D. W. Jun, K. J. Park, Q. Zhang, P. Kaghazchi, D. Aurbach, D. T. Major, G. Goobes, M. Dixit, N. Leifer, C. M. Wang, P. Yan, D. Ahn, K. H. Kim, C. S. Yoon and Y. K. Sun, *Energy Environ. Sci.*, 2018, **11**, 1271–1279.
- 33 P. Cui, Z. Jia, L. Li and T. He, *J. Phys. Chem. Solids*, 2011, **72**, 899–903.
- 34 J. D. Steiner, H. Cheng, J. Walsh, Y. Zhang, B. Zydlewski, L. Mu, Z. Xu, M. M. Rahman, H. Sun, F. M. Michel, C.-J. Sun, D. Nordlund, W. Luo, J.-C. Zheng, H. L. Xin and F. Lin, *ACS Appl. Mater. Interfaces*, 2019, **11**, 37885–37891.
- 35 Y. Kim, *Phys. Chem. Chem. Phys.*, 2019, **21**, 12505–12517.
- 36 O. Breuer, A. Chakraborty, J. Liu, T. Kravchuk, L. Burstein, J. Grinblat, Y. Kauffman, A. Gladkih, P. Nayak, M. Tsubery, A. I. Frenkel, M. Talianker, D. T. Major, B. Markovsky and D. Aurbach, *ACS Appl. Mater. Interfaces*, 2018, **10**, 29608–29621.
- 37 P. Yue, Z. Wang, H. Guo, X. Xiong and X. Li, *Electrochim. Acta*, 2013, **92**, 1–8.
- 38 C. Liang, F. Kong, R. C. Longo, C. Zhang, Y. Nie, Y. Zheng and K. Cho, *J. Mater. Chem. A*, 2017, **5**, 25303–25313.
- 39 K. Min, S.-W. Seo, Y. Y. Song, H. S. Lee and E. Cho, *Phys. Chem. Chem. Phys.*, 2017, **19**, 1762–1769.
- 40 F. Kong, C. Liang, L. Wang, Y. Zheng, S. Peranathan, R. C. Longo, J. P. Ferraris, M. Kim and K. Cho, *Adv. Energy Mater.*, 2019, **9**, 1802586.
- 41 P. Xiao, T. Shi, W. Huang and G. Ceder, *ACS Energy Lett.*, 2019, **4**, 811–818.
- 42 Y. Shin, W. H. Kan, M. Aykol, J. K. Papp, B. D. McCloskey, G. Chen and K. A. Persson, *Nat. Commun.*, 2018, **9**, 4597.
- 43 G. Kresse and J. Furthmüller, *Comput. Mater. Sci.*, 1996, **6**, 15–50.
- 44 G. Kresse and J. Furthmüller, *Phys. Rev. B: Condens. Matter Mater. Phys.*, 1996, **54**, 11169–11186.
- 45 G. Kresse and D. Joubert, *Phys. Rev. B: Condens. Matter Mater. Phys.*, 1999, **59**, 1758–1775.
- 46 J. P. Perdew, K. Burke and M. Ernzerhof, *Phys. Rev. Lett.*, 1996, **77**, 3865–3868.
- 47 J. Cheng, J. Luo and K. Yang, *ACS Appl. Mater. Interfaces*, 2017, **9**, 7682–7690.
- 48 A. Jain, S. P. Ong, G. Hautier, W. Chen, W. D. Richards, S. Dacek, S. Cholia, D. Gunter, D. Skinner, G. Ceder and K. A. Persson, Commentary: The Materials Project: A Materials Genome Approach to Accelerating Materials Innovation, *APL Mater.*, 2013, **1**, 011002.
- 49 E. Cho, S.-W. Seo and K. Min, *ACS Appl. Mater. Interfaces*, 2017, **9**, 33257–33266.
- 50 J. Zhu and G. Chen, *J. Mater. Chem. A*, 2019, **7**, 5463–5474.
- 51 P. W. Tasker, *J. Phys. C: Solid State Phys.*, 1979, **12**, 4977–4984.
- 52 A. W. Moses, H. G. G. Flores, J.-G. Kim and M. A. Langell, *Appl. Surf. Sci.*, 2007, **253**, 4782–4791.
- 53 J. Osorio-Guillen, S. Lany, S. V. Barabash and A. Zunger, *Phys. Rev. Lett.*, 2006, **96**, 107203.
- 54 M. E. Arroyo y de Dompablo, C. Marianetti, A. Van der Ven and G. Ceder, *Phys. Rev. B: Condens. Matter Mater. Phys.*, 2001, **63**, 144107.
- 55 M. E. Arroyo y de Dompablo, A. Van der Ven and G. Ceder, *Phys. Rev. B: Condens. Matter Mater. Phys.*, 2002, **66**, 64112.
- 56 L. Wang, T. Maxisch and G. Ceder, *Phys. Rev. B: Condens. Matter Mater. Phys.*, 2006, **73**, 195107.
- 57 S. Maintz, V. L. Deringer, A. L. Tchougréeff and R. Dronskowski, *J. Comput. Chem.*, 2016, **37**, 1030–1035.
- 58 A. Lücke, U. Gerstmann, T. D. Kühne and W. G. Schmidt, *J. Comput. Chem.*, 2017, **38**, 2276–2282.
- 59 T. Hughbanks and R. Hoffmann, *J. Am. Chem. Soc.*, 1983, **105**, 3528–3537.
- 60 L. Mu, R. Zhang, W. H. Kan, Y. Zhang, L. Li, C. Kuai, B. Zydlewski, M. M. Rahman, C. J. Sun, S. Sainio, M. Avdeev, D. Nordlund, H. L. Xin and F. Lin, *Chem. Mater.*, 2019, **31**, 9769–9776.
- 61 H. Li, A. Liu, N. Zhang, Y. Wang, S. Yin, H. Wu and J. R. Dahn, *Chem. Mater.*, 2019, **31**, 7574–7583.
- 62 T. Weigel, F. Schipper, E. M. Erickson, F. A. Susai, B. Markovsky and D. Aurbach, *ACS Energy Lett.*, 2019, **4**, 508–516.
- 63 Z. Liu, H. Zhen, Y. Kim and C. Liang, *J. Power Sources*, 2011, **196**, 10201–10206.
- 64 H. Arai, S. Okada, Y. Sakurai and J.-i. Yamaki, *Solid State Ionics*, 1998, **109**, 295–302.



- 65 J. R. Dahn, E. W. Fuller, M. Obrovac and U. von Sacken, *Solid State Ionics*, 1994, **69**, 265–270.
- 66 M. Guilmard, L. Croguennec, D. Denux and C. Delmas, *Chem. Mater.*, 2003, **15**, 4476–4483.
- 67 H. J. T. Ellingham, *J. Soc. Chem. Ind.*, 1944, **63**, 125–160.
- 68 J. H. Park, J. Lim, J. Yoon, K. S. Park, J. Gim, J. Song, H. Park, D. Im, M. Park, D. Ahn, Y. Paik and J. Kim, *Dalton Trans.*, 2012, **41**, 3053–3059.
- 69 X. Li, H. Xin, Y. Liu, D. Li, X. Yuan and X. Qin, *RSC Adv.*, 2015, **5**, 45351–45358.
- 70 R. A. House, U. Maitra, L. Jin, J. G. Lozano, J. W. Somerville, N. H. Rees, A. J. Naylor, L. C. Duda, F. Massel, A. V. Chadwick, S. Ramos, D. M. Pickup, D. E. McNally, X. Lu, T. Schmitt, M. R. Roberts and P. G. Bruce, *Chem. Mater.*, 2019, **31**, 3293–3300.
- 71 L. Mu, W. H. Kan, C. Kuai, Z. Yang, L. Li, C. J. Sun, S. Sainio, M. Avdeev, D. Nordlund and F. Lin, *ACS Appl. Mater. Interfaces*, 2020, **12**, 12874–12882.
- 72 L. Croguennec, E. Suard, P. Willmann and C. Delmas, *Chem. Mater.*, 2002, **14**, 2149–2157.
- 73 H. Li, M. Cormier, N. Zhang, J. Inglis, J. Li and J. R. Dahn, *J. Electrochem. Soc.*, 2019, **166**, A429–A439.

